JGR Planets

RESEARCH ARTICLE
10.1029/2022JE007286

Special Section:
ExoMars Trace Gas Orbiter - One Martian Year of Science

Thermal Structure of the Middle and Upper Atmosphere of Mars From ACS/TGO CO_2 Spectroscopy

D. A. Belyaev[1], A. A. Fedorova[1], A. Trokhimovskiy[1], J. Alday[2], O. I. Korablev[1], F. Montmessin[3], E. D. Starichenko[1], K. S. Olsen[4], and A. S. Patrakeev[3]

[1]Space Research Institute (IKI), Moscow, Russia, [2]School of Physical Sciences, The Open University, Milton Keynes, UK, [3]LATMOS/CNRS, Guyancourt, France, [4]Department of Physics, University of Oxford, Oxford, UK

Key Points:

- Seasonal variability of the Martian atmospheric thermal structure at altitudes 20–180 km is reported from CO_2 infrared spectroscopy
- The mesopause altitude rises from 70 to 90 km in the high-winter latitudes to 130–150 km in the summer season for both hemispheres
- The homopause altitude varies from 90 km at aphelion to 130 km at perihelion in the Martian years 34 and 35, and it depends on dust activity

Supporting Information:

Supporting Information may be found in the online version of this article.

Correspondence to:

D. A. Belyaev,
dbelyaev@iki.rssi.ru

Citation:

Belyaev, D. A., Fedorova, A. A., Trokhimovskiy, A., Alday, J., Korablev, O. I., Montmessin, F., et al. (2022). Thermal structure of the middle and upper atmosphere of Mars from ACS/TGO CO_2 spectroscopy. *Journal of Geophysical Research: Planets*, *127*, e2022JE007286. https://doi.org/10.1029/2022JE007286

Received 9 MAR 2022
Accepted 7 OCT 2022

Author Contributions:

Conceptualization: D. A. Belyaev, A. A. Fedorova, O. I. Korablev, F. Montmessin
Data curation: A. Trokhimovskiy, A. S. Patrakeev
Formal analysis: D. A. Belyaev, A. A. Fedorova
Funding acquisition: O. I. Korablev, F. Montmessin
Investigation: D. A. Belyaev, A. A. Fedorova, O. I. Korablev
Methodology: D. A. Belyaev, A. A. Fedorova, J. Alday, E. D. Starichenko

Abstract Temperature and density in the upper Martian atmosphere, above ~100 km, are key diagnostic parameters to study processes of the species' escape, investigate the impact of solar activity, model the atmospheric circulation, and plan spacecraft descent or aerobraking maneuvers. In this paper, we report vertical profiling of carbon dioxide (CO_2) density and temperature from the Atmospheric Chemistry Suite (ACS) solar occultations onboard the ExoMars Trace Gas Orbiter. A strong CO_2 absorption band near 2.7 μm observed by the middle infrared spectrometric channel (ACS MIR) allows the retrieval of the atmospheric thermal structure in an unprecedentedly large altitude range, from 20 to 180 km. We present the latitudinal and seasonal climatology of the thermal structure for 1.5 Martian years (MYs), from the middle of MY 34 to the end of MY 35. The results show the variability of distinct atmospheric layers, such as a mesopause (derived from 70 to 145 km) and homopause, changing from 90 to 100 km at aphelion to 120–130 km at perihelion. Some short-term homopause fluctuations are also observed depending on the dust activity.

Plain Language Summary We report vertical distributions of the density and temperature in the Martian atmosphere in the altitude range from 20 to 180 km. This broad interval of heights embraces regions of the troposphere (<50 km), the mesosphere (50–100 km), and the thermosphere (>100 km). Knowledge of thermal structure in the middle and upper atmosphere (above 50 km) is unique for the Martian climate modeling, studying the atmospheric escape and the impact of solar activity, as well as planning spacecraft maneuvers. Our data are based on remote measurements of the carbon dioxide (CO_2) absorption in the atmosphere at very high altitude resolution of one kilometer. Sensing this major component, 95% of the total density, in the infrared wavelength range allows us to derive the atmospheric temperature as well. We observe the climatology of different atmospheric layers depending on latitude and seasons for 1.5 Martian years, from May 2018 to January 2021. For example, we reveal extremely high variability of the coldest layer, mesopause, from 70 km in the southern winter to 150 km in the southern summer.

1. Introduction

The middle and upper atmosphere of Mars, occupying altitudes above ~50 km, include the mesosphere (60–100 km) and thermosphere, extending higher than ~100 km. This altitude range hosts the temperature minimum of the mesopause at 90–120 km and the homopause, 10–20 km higher, where the atmosphere is no longer uniformly mixed (S. W. Bougher, Brain, et al., 2017). Here, solar ultraviolet (UV) radiation effectively dissociates CO_2 molecules forcing a decrease of its mixing ratio with altitude from 95% to <30% at 170–200 km. At the same time, the mixing ratio of O atoms and CO molecules tends to rise with altitude, decreasing the atmospheric mean molecular mass. Above 200 km, the exobase is the boundary between the collisional and the collisionless atmosphere. Its altitude varies from 200 to 250 km depending on the solar UV flux and the dust loading (Fu et al., 2020; Montabone et al., 2020). In parallel, up-to-date thermospheric models are able to describe how the temperature of the upper atmosphere is affected by temporal variability (diurnal and seasonal) and by solar activity (S. W. Bougher et al., 2015; González-Galindo et al., 2015). The energy to the thermosphere is also supplied by the global circulation and vertical atmospheric waves (González-Galindo et al., 2015; Medvedev et al., 2015). According to models, all the mentioned factors provoke a wide range of temperature variations in the upper thermosphere, from 150 to 350 K.

A number of experiments have explored the structure and dynamics of the Martian upper atmosphere for a few decades: Either in situ or using the orbital limb sounding in emission or absorption spectrometry. Among the in

Project Administration: A. Trokhimovskiy, O. I. Korablev, F. Montmessin, A. S. Patrakeev
Resources: A. Trokhimovskiy, O. I. Korablev
Software: D. A. Belyaev
Supervision: O. I. Korablev, F. Montmessin
Validation: D. A. Belyaev, A. A. Fedorova, J. Alday, F. Montmessin, E. D. Starichenko, K. S. Olsen
Visualization: D. A. Belyaev
Writing – original draft: D. A. Belyaev, J. Alday, O. I. Korablev, K. S. Olsen

situ, the accelerometry profiles of integrated density were measured on board entry probes, Mars-6 (Avduyevskiy et al., 1975) and Viking 1 and 2 (Seiff & Kirk, 1976) in the 1970s, as well as Mars Pathfinder in 1997 (Withers et al., 2003). During the Viking descents, the temperature and density of major constituents were also probed by the neutral mass-spectrometers (Nier & McElroy, 1977). At the turn of the century, aero-braking campaigns of Mars Global Surveyor (MGS), Mars Odyssey, and Mars Reconnaissance Orbiter spacecraft resulted in the first prolonged data set describing the thermospheric temperature and density variations (S. W. Bougher, Brain, et al., 2017; Keating et al., 1998; Withers, 2006). The Spectroscopy for Investigation of Characteristics of the Atmosphere of Mars (SPICAM) instrument on board Mars Express sounded the mesospheric and thermospheric altitudes (30–150 km) in stellar occultations in the UV CO_2 absorption band (110–200 nm) (Forget et al., 2009; Quemerais et al., 2006). SPICAM has also revealed several cases of the CO_2 supersaturation condition around the mesopause, observed together with detached aerosol layers interpreted as CO_2 ice clouds forming below 100 K (Montmessin et al., 2006).

A new era of thermosphere climatology has begun with the Mars Atmosphere and Volatile EvolutioN (MAVEN) orbiter, exploring the upper atmosphere since 2014. The Neutral Gas and Ion Mass Spectrometer (NGIMS) (S. W. Bougher, Roeten, et al., 2017; Stone et al., 2018) and the accelerometer (ACC) (Zurek et al., 2017) measured the density in situ down to 120 km during regular "deep dip" maneuvers (S. Bougher et al., 2015). Remotely, the Imaging Ultraviolet Spectrograph (IUVS) sounded the atmospheric structure either from the limb UV dayglow (Jain et al., 2021) or nightside stellar occultations (Gröller et al., 2018). IUVS observed limb airglow of the CO_2^+ UV doublet at 290 nm and, as a result, derived mesospheric and thermospheric interannual variations of the temperature from January 2015 to July 2020 that covered three Martian Years (MYs), from the MY 32 perihelion ($L_S = 250°$) to the MY 35 perihelion seasons (Jain et al., 2021). Star occultations were performed with a broad spatial coverage for longitude, latitude, local time (LT), and season, from March 2015 ($L_S = 315°$, MY 32) to April 2018 ($L_S = 165°$, MY 34), and counting >600 temperature altitude profiles in the range 20–140 km with the vertical sampling better than 6 km. Based on this data set, Nakagawa et al. (2020) revealed a warm layer in the nightside low-latitude mesosphere (70–90 km) during the northern summer. One more data set, from the MAVEN Extreme Ultraviolet Monitor (EUVM) solar occultations, revealed the density and temperature variations in the thermosphere (120–200 km) depending on solar EUV radiation (Thiemann et al., 2018).

The ExoMars Trace Gas Orbiter (TGO) was inserted into orbit in October 2016. The spacecraft performed an aero-braking campaign from March 2017 to February 2018 while the onboard accelerometers were measuring the density variations in the lower thermosphere (100–130 km, Forbes et al., 2021; Jesch et al., 2019). The nominal TGO science mission began just after, with remote atmospheric measurements of strong CO_2 absorption bands in the solar occultation mode by high-resolution infrared (IR) spectrometers (Korablev et al., 2018; Vandaele et al., 2018).

In this paper, we report highly sensitive measurements of the temperature and density vertical distribution using the Atmospheric Chemistry Suite (ACS) on board TGO in the regime of solar occultation (Korablev et al., 2018). The middle-IR channel (ACS MIR) has been performing the experiment since April 2018 in the spectral range from 2.3 to 4.2 μm with a resolving power exceeding 25,000 and the vertical resolution about ∼1 km. The instrument senses the CO_2 absorption band around 2.7 μm in an extremely wide altitude range, from 20 to 180 km, covering the troposphere, the mesosphere, and the thermosphere of Mars. We describe a scheme of the temperature and density retrievals validating with simultaneous measurements of the CO_2 band at 1.58 μm by the near-IR channel (ACS NIR) below 100 km (Fedorova et al., 2020, 2022). The presented observations include more than 600 vertical profiles spreading over 1.5 MYs, from the middle of MY 34 to the end of MY 35. The data set allows observing long-term and latitudinal variations of the thermal structure in the middle-upper atmosphere (above ∼40 km) at the dawn and dusk terminators.

2. ACS MIR Solar Occultation Measurements

2.1. ACS MIR Spectra

ACS is a set of three IR spectrometers devoted to study chemical composition as well as aerosol and thermal structure of the Martian atmosphere on board the ExoMars TGO mission (Korablev et al., 2018). ACS MIR is a cross-dispersion echelle spectrometer dedicated to solar occultation measurements in the 2.3–4.3 μm wavelength range. Each occultation session is performed at 1 of 10 angular positions of the MIR secondary grating

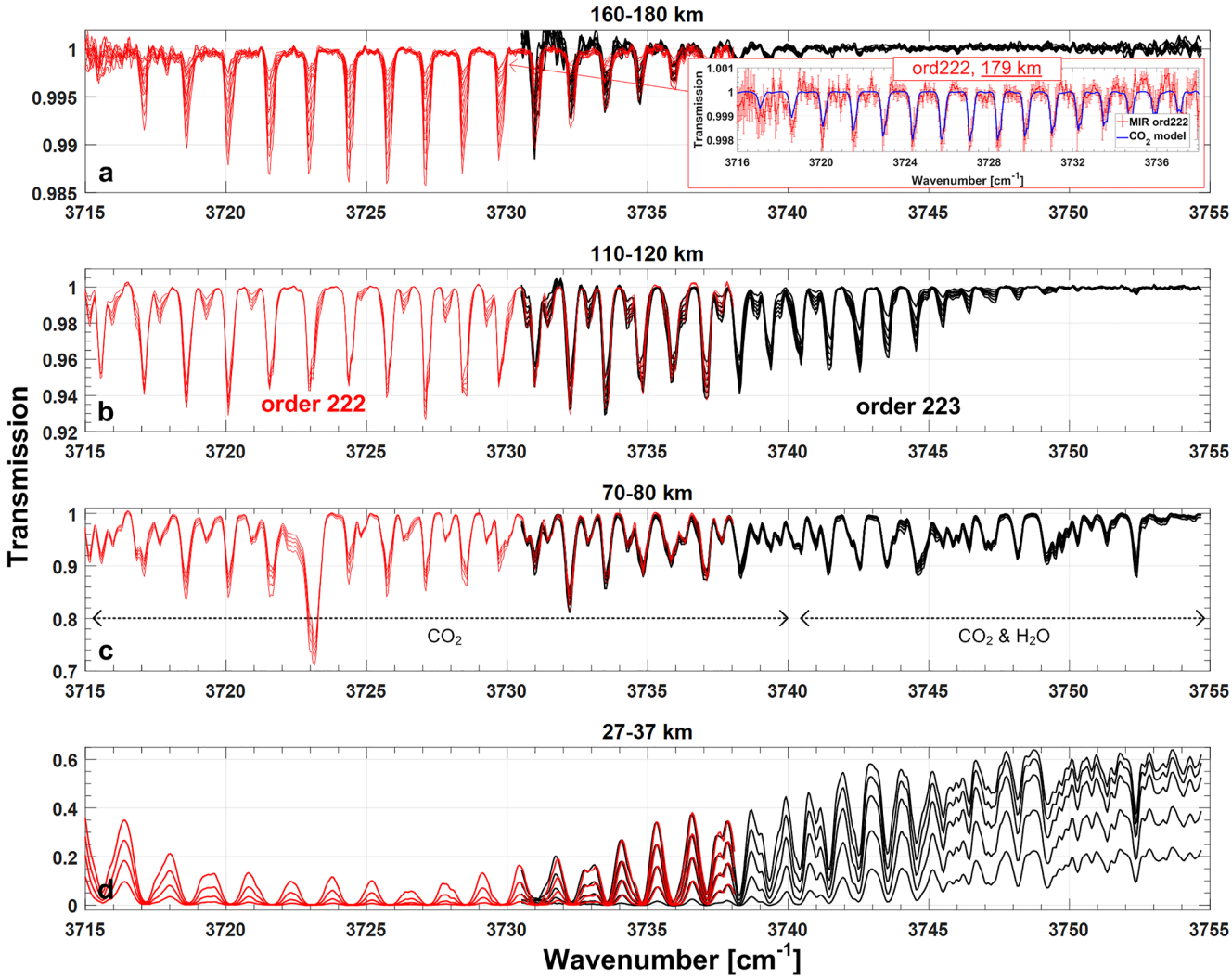

Figure 1. Set of transmission spectra measured by Atmospheric Chemistry Suite MIR during one occultation at the orders #222 (in red) and #223 (in black) on the tangential altitude ranges (a) 160–180, (b) 110–120, (c) 70–80, and (d) 27–37 km. Each tiny curve (spectrum) corresponds to a specific altitude. An individual spectrum with error bars in the red frame on panel (a) is one from the order #222 measured at 179 km and compared with a corresponding CO_2 model (in blue) (see Section 3). The data corresponds to orbit 3820n2 (1 October 2018, MY 34, $L_S = 260.9°$, latitude −55.3°, longitude 53.9°, and local time 20.8).

that disperses and spatially separates about 10–15 echelle diffraction orders. These are recorded simultaneously with an HgCdTe focal plane array (FPA) that is 640 × 512 pixels. The spectral range of interest, 2.66–2.7 μm, lies within the diffraction orders #222 and #223 at the secondary grating position #4. One order covers a spectral interval of about 30 cm^{-1} (~25 nm); a spectrum is dispersed along 640 elements with a spectral sampling of 0.05 cm^{-1} and the resolving power $\lambda/\delta\lambda$ reaching ~25,000 (i.e., ~0.15 cm^{-1} of spectral resolution). In the occultation field-of-view (FOV), the instrumental rectangular slit cuts a part from the solar disk, so that one order occupies a stripe with about 20 FPA rows. In such a manner, the sequence of orders are located on the matrix as stripe-by-stripe, one above the other, with some dark rows between them (see in Alday, Wilson, et al. (2021)). For our analysis, we selected one row from each of two adjacent stripes correspondent to the orders #222 and #223. The considered rows relate to the highest signal-to-noise ratio (SNR) in order #223 and to minimum "doubling" effect (double Gaussian instrumental line shape (ILS)) in order #222 (Alday et al., 2019).

The data to be analyzed is a set of transmissions spectrally registered and calibrated separately for every occultation with the corresponding ancillary geometry for each spectrum (Figure 1). Geometrical coordinates of the observed target (tangential) point are calculated at the closest distance from the surface to the instrument's line-of-sight (LOS). The transmission is obtained by division of the solar spectrum passed through the atmosphere to the

reference spectrum, which is measured above the tangential altitude of 200 km, where an influence of the atmospheric absorption at 2.7 μm is negligibly small for the instrument. Depending on the integration time (∼1 s) and occultation geometry, atmospheric spectra are measured with an altitude sampling ranging from 0.5 to 2.5 km, which provides well-resolved vertical profiling for an atmosphere whose scale height is around 10 km. The ACS MIR FOV projected at the limb is estimated at around 1–3 km in terms of altitude.

Spectral calibration for measured transmissions includes a pixel-to-wavenumber alignment and a determination of the ILS. Both procedures were performed for each MIR order independently since dispersion of light onto the FPA varied from row to row. The details for the order #223 are presented in papers by Belyaev et al. (2021) and Alday, Trokhimovskiy, et al. (2021), dedicated to the retrieval of water vapor abundance. For order #222, the algorithm was analogous, using spectra above 100 km (Figures 1a and 1b) where CO_2 absorption lines are thin (in the low-pressure atmosphere) and still deep enough for the precise calibration. In Figure 1, both calibrated ACS MIR orders are bonded in one set of spectra with an intersection between 3,731 and 3,738 cm^{-1}. Spectral parts toward the side of the FPA of all orders are noisy (i.e., 3,715–3,717 cm^{-1} for #222 and 3,731–3,733 cm^{-1} for #223 in Figure 1a) because the blaze function of the echelle grating gives relatively low SNR onto the edges of FPA. The central parts are clearer, and the SNR varies between 1,000 and 5,000, which corresponds to transmission uncertainties below 0.001 (Figure 1a).

2.2. Data Coverage

The analyzed measurements cover a period of 1.5 MYs, the second half of MY 34 and the whole of MY 35, that correspond to ACS MIR observations from May 2018 to January 2021. The selected data set (all the secondary grating position #4 observations) comprises 308 occultation sessions in the Northern Hemisphere and 301 sessions in the Southern Hemisphere, encompassing seasonal periods from L_S = 180°–355° in MY 34 and from L_S = 2°–356° in MY 35. Due to the solar occultation geometry the instrument's LOS tangentially crosses the planetary terminator either at sunset or at sunrise, sounding morning and evening twilight of the atmosphere (Figure 2a). Geography of the tangent point varies slowly during one occultation, less than 3° of latitude or longitude. Thus, we estimate the coordinates averaging them over the tangential altitudes from 0 to 200 km. The observations are mainly concentrated at high latitudes, 40°–80°, in both hemispheres, while the longitudinal distribution of the tangent points is uniform over the planet (Figure 2b). The latitudinal coverage depending on the solar longitude is presented in Figure 2c, characterizing the seasons of MY 34 and MY 35 perihelion (L_S = 240°–300°) and MY 35 aphelion (L_S = 60°–120°) with in-between Martian seasons.

During the period covered by the measurements, different dust events affected Mars: The global dust storm (GDS) at L_S = 190°–240° in MY 34, the C storms at L_S = 320°–330° in both MY 34 and 35, and the B storm at L_S = 240°–270° in MY 35. The regional B and C storms encompassed almost the whole Southern Hemisphere and the low latitudes of the Northern one (gray frames in Figure 2c) as seen from the Mars Climate Sounder observations presented by Montabone et al. (2020) and Olsen et al. (2021).

3. Retrievals of CO_2 Density and Temperature

3.1. CO_2 Spectroscopy at 2.7 μm

The selected CO_2 absorption lines, the short wavelength part of the 2.7 μm band, lie in the ACS MIR echelle orders #222, with the strongest transitions at 3,715–3,737 cm^{-1} and #223 at 3,732–3,755 cm^{-1} (Figure 3). These lines are partially mixed with H_2O (and its isotopologues) absorption bands, which are taken into account in this work by the same manner as in the previous ACS MIR retrievals of Belyaev et al. (2021) and Alday, Trokhimovskiy, et al. (2021). Figure 3 shows absorption cross sections, σ, of CO_2 and H_2O in our spectral range of interest, including rotational lines with intensities significantly dependent on temperature. The cross sections were calculated line-by-line based on the HITRAN2016 database (Gordon et al., 2017) with self-broadening for CO_2 lines. The broadening parameters of the CO_2-rich atmosphere for the water lines were taken from Gamache et al. (2016) and Devi et al. (2017). The cross section derivatives in Figure 3b demonstrate the various temperature behaviors of the major considered lines, possessing either positive or negative signs. Thanks to that, an independent and simultaneous retrieval of temperature and molecular concentrations is possible.

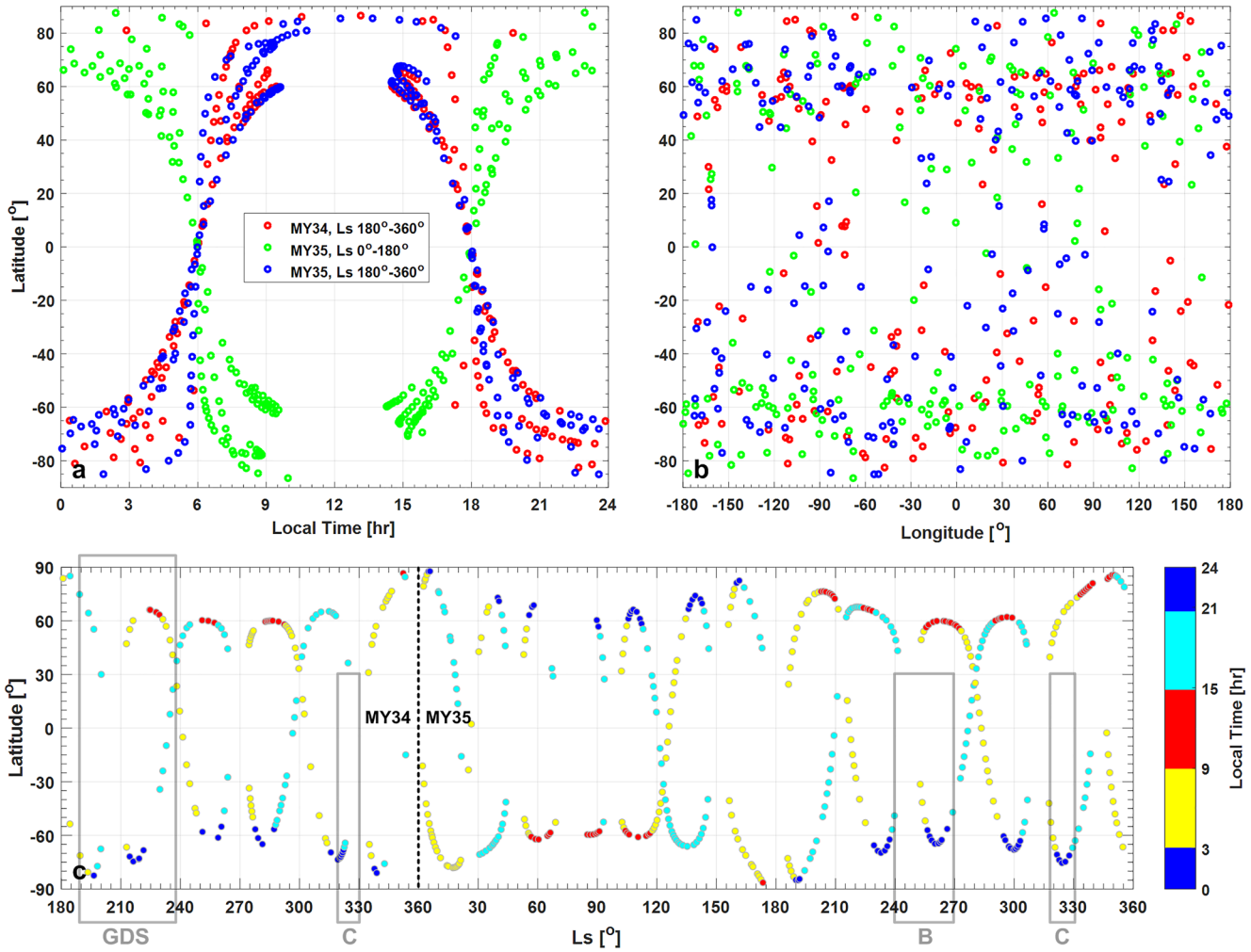

Figure 2. Geographical distributions of the tangent points for the Atmospheric Chemistry Suite MIR solar occultations at the grating position #4 covering the 2.7 μm band. The coordinates are latitude versus (a) local time, (b) longitude, and (c) solar longitude, L_S. The data in panels (a and b) are combined in annual periods: Second half of MY 34 (red), first half of MY 35 (green), and second half of MY 35 (blue). The data at panel (c) are color-coded by intervals of local time in hours (hr): 3–9 (yellow), 9–15 (red), 15–21 (purple), and 21–3 hr (blue). Each circle corresponds to one occultation with related coordinates of the tangential point. Gray frames in panel (c) outline periods of the global dust storm and the C storm in MY 34 and the B and C storms in MY 35.

3.2. Retrieval Concept

In order to simultaneously derive density and temperature at a specified altitude, we applied a multi-iteration scheme by fitting a modeled transmission spectrum to the measured one. The details of this method are described in Supporting Information S1 and also in the paper of Belyaev et al. (2021). Here, we assume the hydrostatic equilibrium, to derive the pressure from the retrieved temperature and density profiles, where the atmospheric mean molecular mass is taken from the Mars Climate Database (MCD 5.3; Millour et al., 2018) adapted for the ACS occultation geometry.

The applied retrieval algorithm was performed for orders #222 and #223 separately since they require different calibration parameters with unique ILSs. Vertical profiles from order #223 were derived by Belyaev et al. (2021) and validated with analogous schemes, such as the one adopted by Alday, Trokhimovskiy, et al. (2021) using the NEMESIS algorithm and the one from ACS NIR (Fedorova et al., 2022) for simultaneous occultations at altitudes below 100 km. Comparison between the present MIR and the NIR temperature profiles is shown in Figure S1 in Supporting Information S1, where a good consistency within ~10 K is seen in frames of the average measurement errors about 5–10 K (see also Figures 4b, 4f and 4j). The profiles retrieved from order #223 are sensitive to altitudes from 5–20 km to 140–160 km (depending on season), while the profiles from #222 are sensitive to an

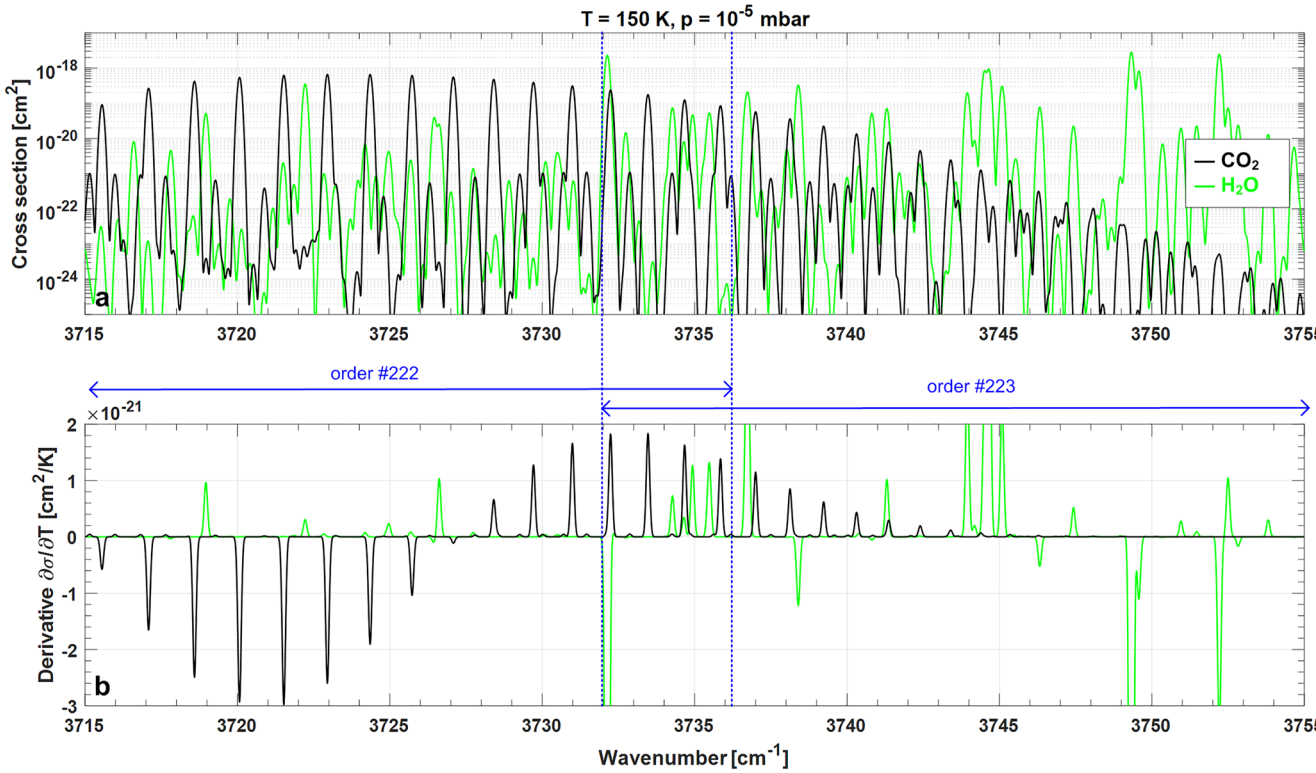

Figure 3. Absorption spectroscopy at the 2.66–2.69 μm wavelength range. (a) Cross sections, σ, for molecules of CO_2 (in black) and H_2O (in green) convolved by the instrumental line shape. (b) Partial derivatives of cross section with respect to temperature ($\partial\sigma/\partial T$). Cross sections were calculated for the temperature $T = 150$ K and pressure $p = 10^{-5}$ mbar, typical for the upper mesosphere at ~100 km.

altitude range ~20 km higher due to the stronger CO_2 lines. One of the uppermost transmission fits is presented in Figure 1a (zoomed inset) with the absorption line depth not exceeding 0.2%. The lowest and the uppermost heights for an individual profile are established according to the retrieval uncertainties. These are estimated from the transmission errors and by the partial derivatives for all free parameters. We selected only the values corresponding to temperature error bars below 20 K. Final density and temperature profiles are obtained by "binding" those from both orders with a weighted average in the intersecting altitude interval. For the temperature (Figures 4a, 4e and 4i), the weighted mean $T_{\text{mean}} = (T_{222}w_{222} + T_{223}w_{223}) / (w_{222} + w_{223})$, where the weighting factor w is the inverse square of the measurement error, $w_i = 1/\sigma_i^2$.

Together with the molecular abundance, we derive the aerosol slant opacity when fitting this parameter at the short wavelength edge of the order #223, that is, at 3,753–3,755 cm^{-1}, where the gaseous absorption is minimal (Figure 1). In our case, the opacity indicates the atmospheric aerosol loading along the LOS of ACS, expressing periods of the dust activity. Figure 4 demonstrates the retrieved vertical profiles from three different seasons: The GDS of MY 34 (Figures 4a–4d), perihelion of MY 34 (Figures 4e–4h), and aphelion of MY 35 (Figures 4i–4l) at the middle and high latitudes of the Southern Hemisphere. In the first two cases, the lower atmosphere is warmer (Figures 4b, 4f and 4j), denser (Figures 4c, 4g and 4k), and more dusty (Figures 4d, 4h and 4l) than in the third (aphelion) case. During the GDS of 2018 (Montabone et al., 2020) the aerosol slant opacity reaches high values of 2–3 between 40 and 50 km (Figure 4d), where the corresponding temperature rises up to 200 K (Figure 4b). Perihelion, which occurs during the southern summer, is a period with intensified atmospheric warming and upwelling accompanied by increased density and aerosol opacity (Figures 4f–4h). At the aphelion season, southern winter, the situation is opposite, with a colder and more transparent atmosphere (Figures 4j–4l).

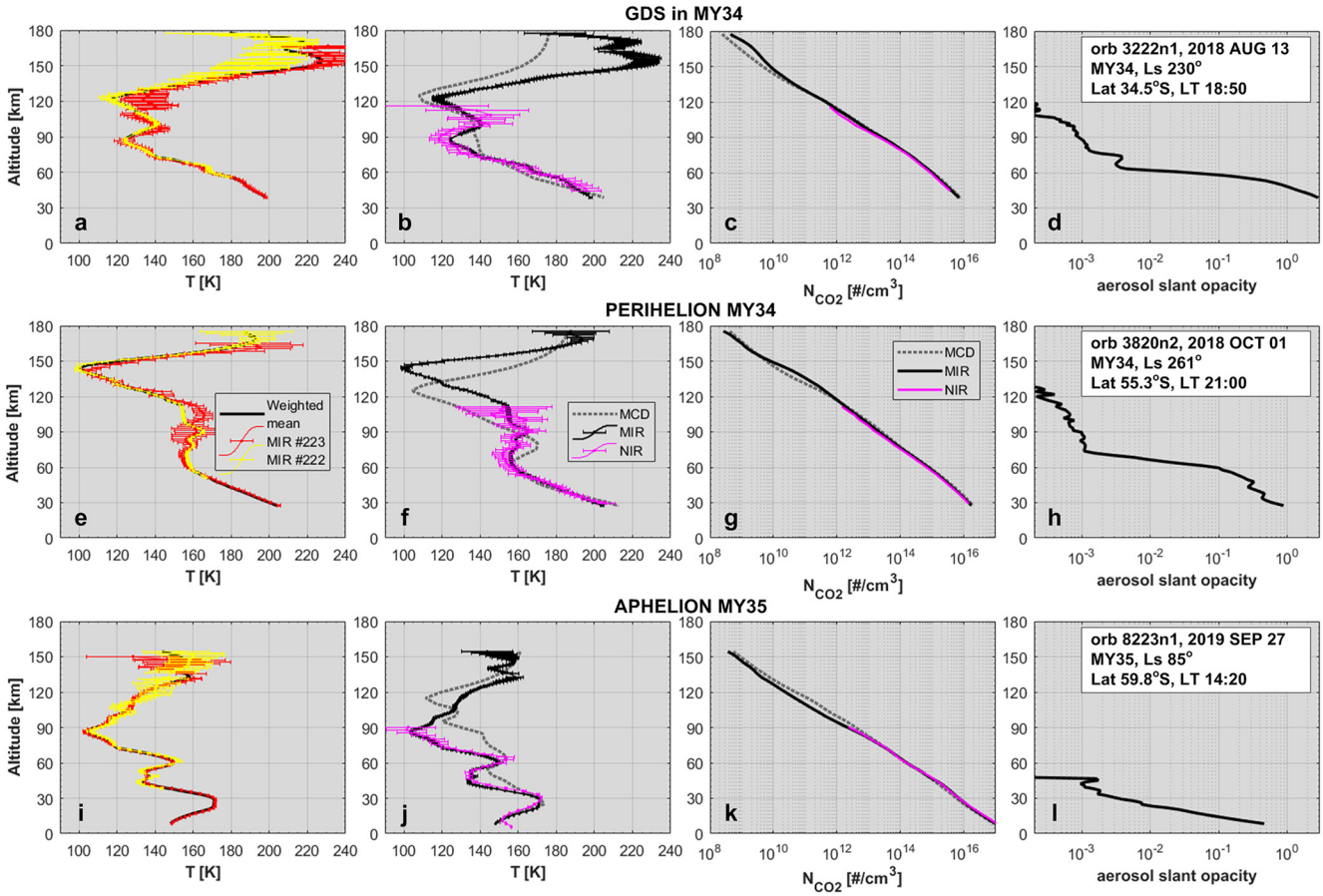

Figure 4. (a, b, e, f, i, and j) Individual vertical profiles of temperature, (c, g, and k) CO_2 number density, and (d, h, and l) aerosol slant opacity retrieved from Atmospheric Chemistry Suite (ACS) MIR occultations in the Southern Hemisphere at different periods: (a–d) global dust storm in MY 34 (L_S = 230°), (e–h) near perihelion in MY 34, and (i–l) near aphelion in MY 35. Panels (a, e, and i) comparison between ACS MIR orders #222 (yellow) and #223 (red) with their weighted mean temperatures (black). Panels (b, f, and j): comparison of the ACS MIR temperature profiles (black) with the ACS NIR ones (magenta; Fedorova et al., 2022) and with the MCD5.3 climatology predictions (gray). Panels (c, g, and k) analogous comparison for CO_2 number density.

4. Results

4.1. Mesopause and Subfreezing Temperatures

In each individual vertical profile of the temperature, one can derive the coldest extremum that characterizes the atmospheric mesopause (see examples in Figures 4b, 4f and 4j). Over the whole data set, the altitude of the mesopause varies in a broad range, from 70 to 145 km (Figure 5a). The lowest altitudes (<100 km) take place in the equatorial region close to equinoxes. During the solstice seasons the mesopause also gets down to 70–90 km in the winter hemisphere, especially around aphelion. On the other hand, the uppermost heights (>120 km) occur in the summer time at high latitudes, mostly in the south at perihelion. Such a high altitude variability relates to a change of the retrieved CO_2 number density (and pressure) by four orders of magnitude: From ~10^{10} cm^{-3} (10^{-5} Pa) at 145 km to ~10^{14} cm^{-3} (0.1 Pa) at 70 km. To compare, the altitude of a constant density level around mesopause, 10^{12} cm^{-3}, varies with less contrast: From ~90 km at aphelion to ~120 km at perihelion (Figure 5b). It is driven by nominal seasonal atmospheric contraction/expansion between aphelion and perihelion. Thus, there are additional effects of the atmospheric circulation causing extremely low and high mesopause altitudes.

Meridional winds, effectively acting around the upper mesosphere and the lower thermosphere, could be a possible source of the mesopause variation. The general circulation model of González-Galindo et al. (2009) describes an interhemispheric airmass transport from the summer (southern) hemisphere to the winter (northern) one at L_S = 270°–300°. For this season, the model predicts a vertical upward wind from the mesosphere to the thermosphere on the south and the downward one on the north. It results in the altitude variations between 90 and

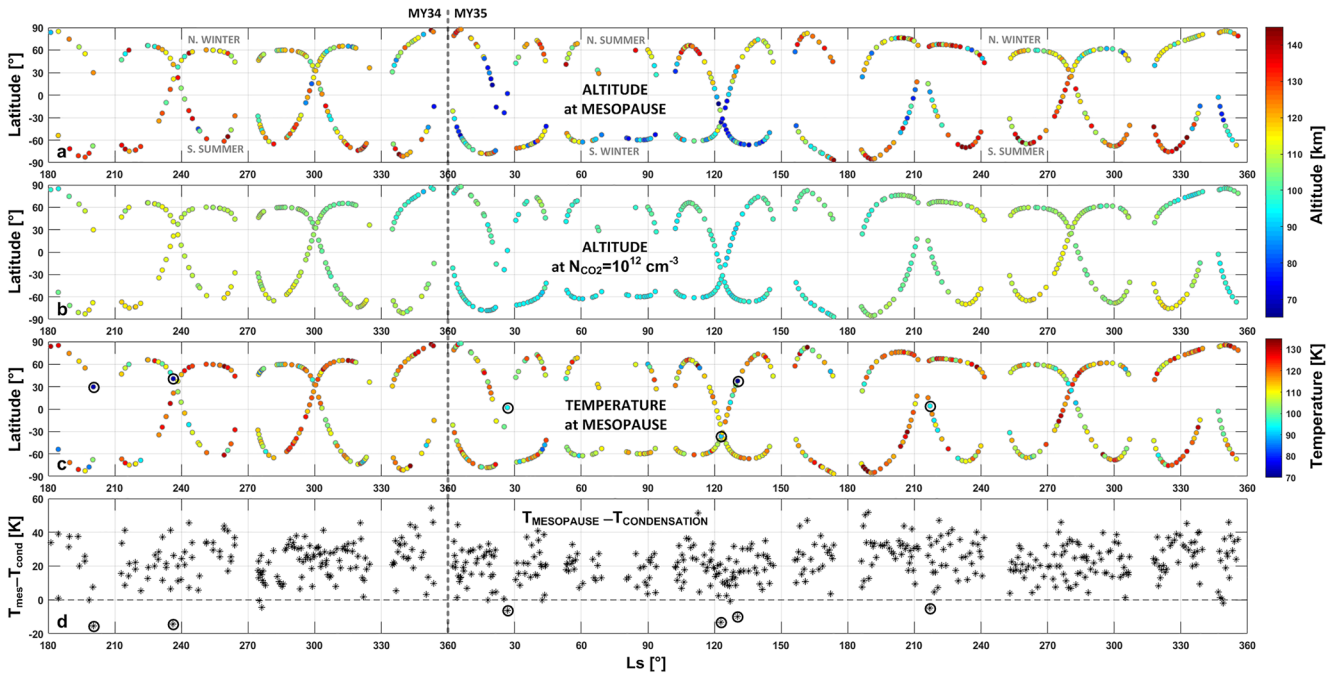

Figure 5. Distribution of the mesopause (a) altitude and (c) temperature with latitude and solar longitude (L_S) derived from Atmospheric Chemistry Suite MIR solar occultations for 1.5 MYs. Panel (b) analogous distribution of the altitude at the constant density level $N_{CO2} = 10^{12}$ cm^{-3}. Panel (d) seasonal (L_S) variation of the mesopause temperatures (T_{mes}) related to the temperature of CO_2 condensation (T_{cond}) at the mesopause level. Six events when $T_{mes} - T_{cond} < -5$ K are pointed by circles (c and d).

130 km observed by ACS-MIR at $L_S = 240°$–$300°$ in both MY 34 and MY 35 (Figure 5a) that corresponds to the modeled mesopause pressure variability in the range of 10^{-4}–10^{-2} Pa (González-Galindo et al., 2009). The reverse airmass motion in the southern winter could provide the higher altitude contrast, 70–140 km, observed at $L_S = 90°$–$150°$ (Figure 5a). Another source could be an effect of CO_2-radiation cooling at 15 μm band described by Medvedev et al. (2015).

The derived mesopause temperature varies mostly in the range of 90–130 K with a few extremely cold points below 90 K in the near-equatorial region (Figure 5c) that could indicate subfreezing CO_2 conditions. The observed temperature and CO_2 density allows us to estimate directly the temperature of CO_2 condensation T_{cond}. We applied the following formula, adapted from Washburn (1948) and used by Forget et al. (2009) for SPICAM data set: $T_{cond} = -3148/(\ln(0.01 \cdot T \cdot \rho \cdot R) - 23.102)$, with ρ the CO_2 mass density (kg/m^3) and $R = 192$ m^2/(s^{2}K) the gas constant for Mars. Considering the observed mesopause temperatures related to T_{cond}, we revealed six events when the difference $T - T_{cond}$ gets below −5 K (Figure 5d). These cases point out to the supersaturation conditions where CO_2 ice clouds may potentially form. All of them occupy low latitudes (see in Figure 5c) and correspond to the morning atmosphere, except for the one at $L_S = 200°$of MY 34 relating to the evening during GDS. The vertical temperature profiles for those six examples are shown in Figure S2 in Supporting Information S1 on a background of the corresponding condensation profiles.

The subfreezing CO_2 temperatures at such a low mesopause pressure were previously observed by SPICAM nightside occultations accompanied with signatures of CO_2 ice absorption in the UV spectra (Montmessin et al., 2006). In parallel, OMEGA imaging spectrometer also observed the high altitude CO_2 ice clouds in the reflectance spectroscopy around 4.26 μm (Montmessin et al., 2007). Both, SPICAM and OMEGA, revealed such clouds near the equator before and after northern summer solstice (Forget et al., 2009) that coincides with our observations at $L_S = 20°$–$200°$ (Figures 5c and 5d). SPICAM also characterized the mesopause temperature and pressure distribution showing analogous ranges of the variability: 80–130 K and 10^{-4}–10^{-2} Pa (Forget et al., 2009).

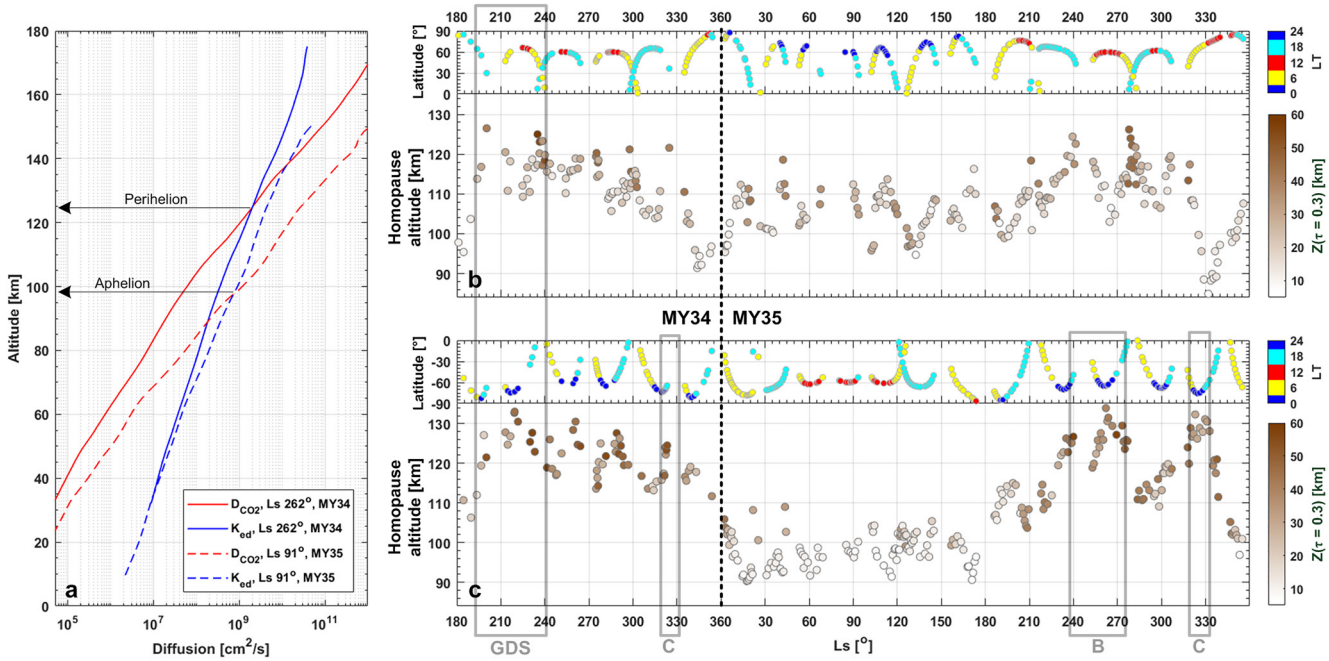

Figure 6. Revealing of the homopause altitude from the Atmospheric Chemistry Suite MIR occultations for 1.5 MYs. (a) Vertical profiles of the molecular (D_{CO2}, in red) and eddy (K_{ed}, in blue) diffusion coefficients retrieved from the observations at perihelion MY 34 (solid lines) and aphelion MY 35 (dashed lines). Black arrows point to the definition of the homopause heights. (b) Distribution of the homopause altitude versus solar longitude (L_S) in the Northern Hemisphere; the color code corresponds to an altitude (Z) where the aerosol slant opacity (τ) equals 0.3. The data are supplemented by the latitudinal coverage taken from Figure 2c. (c) Panel (b) shows the same for the Southern Hemisphere. Gray frames outline periods of the global dust storm and the C storm in MY 34 and the B and C storms in MY 35.

4.2. Homopause Altitude

The atmospheric homopause is the boundary between the homosphere, where the gaseous species are uniformly mixed with a common scale height, and the heterosphere, where a diffusive separation of minor species occurs with individual scale heights. The homopause altitude can be quantitatively determined when the eddy diffusion coefficient, which is dominant in the homosphere, equals the molecular diffusion coefficient, prevailing in the heterosphere. We calculated the vertical distribution of those coefficients from the retrieved density and temperature altitude profiles. Depending on a height, z, the eddy diffusion was estimated from 1-D models of Krasnopolsky (2019): $K(z) = K_0 \cdot \sqrt{n(35\,\text{km})/n(z)}$. The tropospheric eddy K_0 is equal to 10^7 cm^2/s at z = 35 km as it was recommended by Rosenqvist and Chassefière (1995). The total number density $n(z) = p(z)/(k_B \cdot T(z))$, where k_B is Boltzmann constant, $T(z)$ is the temperature, and $p(z)$ is the hydrostatic pressure derived from the retrievals. If the lowest retrieved point exceeded 35 km, we linearly extrapolated the density profile (in log scale) down to 35 km, in order to reach the value n (35 km).

The molecular diffusion coefficient D_{CO2}, being defined by the kinetic energy of molecule, is proportional to the free molecular path $l_{CO2}(z) = (Q_{CO2} \cdot n_{CO2}(z))^{-1}$ and to the mean thermal speed $v^{th}_{CO2}(z) = \sqrt{3 \cdot k_B \cdot T(z) \cdot N_A / M_{CO2}}$, where Q_{CO2} is the CO_2 effective gas-kinetic cross section (0.52 nm^2), N_A is Avogadro number, and M_{CO2} is the CO_2 molar mass (44.01 g/mol). The complete expression is $D_{CO2}(z) = \frac{300\pi\sqrt{2}}{16} \cdot l_{CO2}(z) \cdot v^{th}_{CO2}(z)$ as it is described by Jacobson (2005, pp. 102–528) and adopted by Piccialli et al. (2015) for the CO_2-rich atmosphere of Venus.

Examples of the derived $K(z)$ and $D_{CO2}(z)$ profiles for the ACS MIR occultations at perihelion and aphelion are presented in Figure 6a. The homopause point is the height where correspondent $K(z)$ and $D_{CO2}(z)$ curves cross each other. In general, analyzing over 1.5 MYs, this altitude varies from 90 to 100 km around aphelion to 115–125 km around perihelion in the Northern Hemisphere (Figure 6b) and more widely, to 125–135 km, in the Southern Hemisphere (Figure 6c). Those local peaks in the general trends seem to correlate with the higher aerosol loading related to the dust seasons. It is expressed by an altitude level where the slant opacity equals 0.3 (i.e., ~75% of transmission). The higher this level, the denser the atmospheric aerosol densities, as can be estimated from the opacity profiles in Figures 4d, 4h and 4l. The homopause fluctuations are also defined by the latitudinal

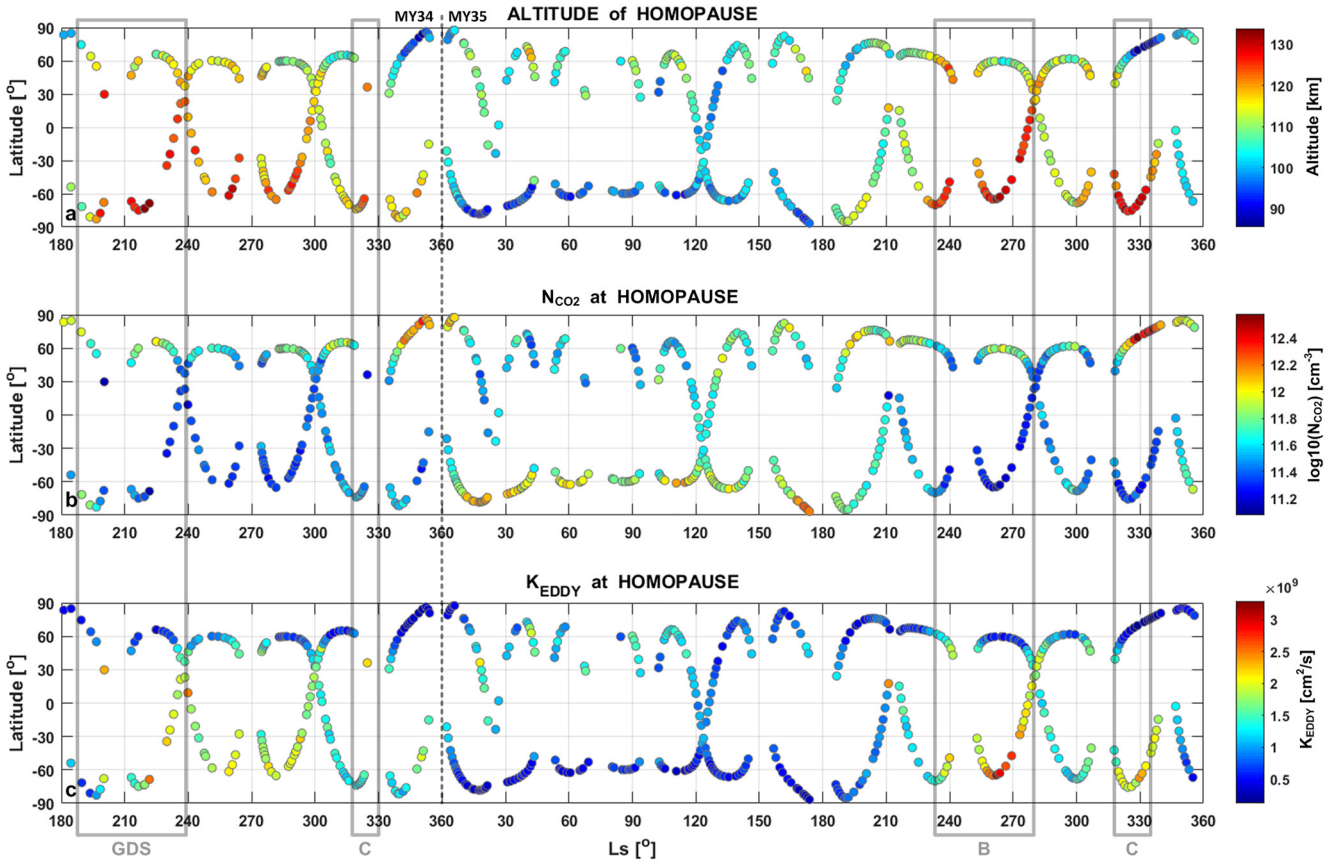

Figure 7. Maps of the homopause distribution with latitude and solar longitude (L_S) derived from Atmospheric Chemistry Suite-MIR solar occultations for 1.5 MYs. (a) Color codes are for the altitude, (b) CO_2 number density N_{CO2}, and (c) the eddy diffusion coefficient K_{EDDY}. Gray frames outline periods of the global dust storm and the C storm in MY 34 and the B and C storms in MY 35.

coordinates, as seen from the data coverage in Figures 6b and 6c. One can notice that some points at GDS and regional storms correspond to less aerosol opacity than outside these periods (Figures 6b and 6c). Those observations lie near polar regions, distantly from the equatorial epicenter of dust storms, as is shown by Montabone et al. (2020) and seen in Figures 8a and 8c of the present paper.

Maps of the homopause distribution with latitude and solar longitude are presented in Figure 7 for the altitude, the derived CO_2 number density, and the eddy diffusion coefficient K_{ed}. The uppermost heights, above 120 km, correspond precisely to the location of dust events and to southern summer seasons, that is, perihelion (Figure 7a). The lowest homopause, below 100 km, occurs near the equinox polar regions in the morning twilight and at high southern winter latitudes, that is, aphelion. At the same time, the number density at homopause varies reversely: From 10^{11} cm^{-3} at high altitudes to $3{\cdot}10^{12}$ cm^{-3} at low altitudes (Figure 7b). The homopause behavior of the diffusion coefficient correlates with the altitude distribution: Increasing above $2{\cdot}10^{9}$ cm^2/s during the stormy and summer seasons and getting below $5{\cdot}10^{8}$ cm^2/s at high latitudes of winter and equinox periods (Figure 7c). An exception is C storm of MY 34, which was concentrated mainly at latitudes less than 60° (Montabone et al., 2020) that almost were not covered by our measurements at L_S = 320°–330°.

Alday, Wilson, et al. (2021) also retrieved the altitude of homopause from the ACS MIR occultations when analyzing the fractionation by diffusive separation using vertical profiles of $^{13}C/^{12}C$ and $^{18}O/^{16}O$ isotopic ratios in CO_2. The derived height occurred to be 95 ± 2 km on average, which is consistent with our results. NGIMS onboard the MAVEN spacecraft observed the homopause variability during 2015–2016, between L_S = 300° in MY 32 and L_S = 250° in MY 33, using the density ratio of N_2 to Ar (Slipski et al., 2018). The minimum altitude was established at 70 km in the aphelion season and the maximum at 130 km in the perihelion one, with the variability of homopause CO_2 density by 3 orders of magnitude, 10^{10}–10^{13} cm^{-3}. Here, the perihelion altitude agrees with our uppermost values about ∼130 km, while the aphelion one is ∼20 km lower than the MIR results. On the

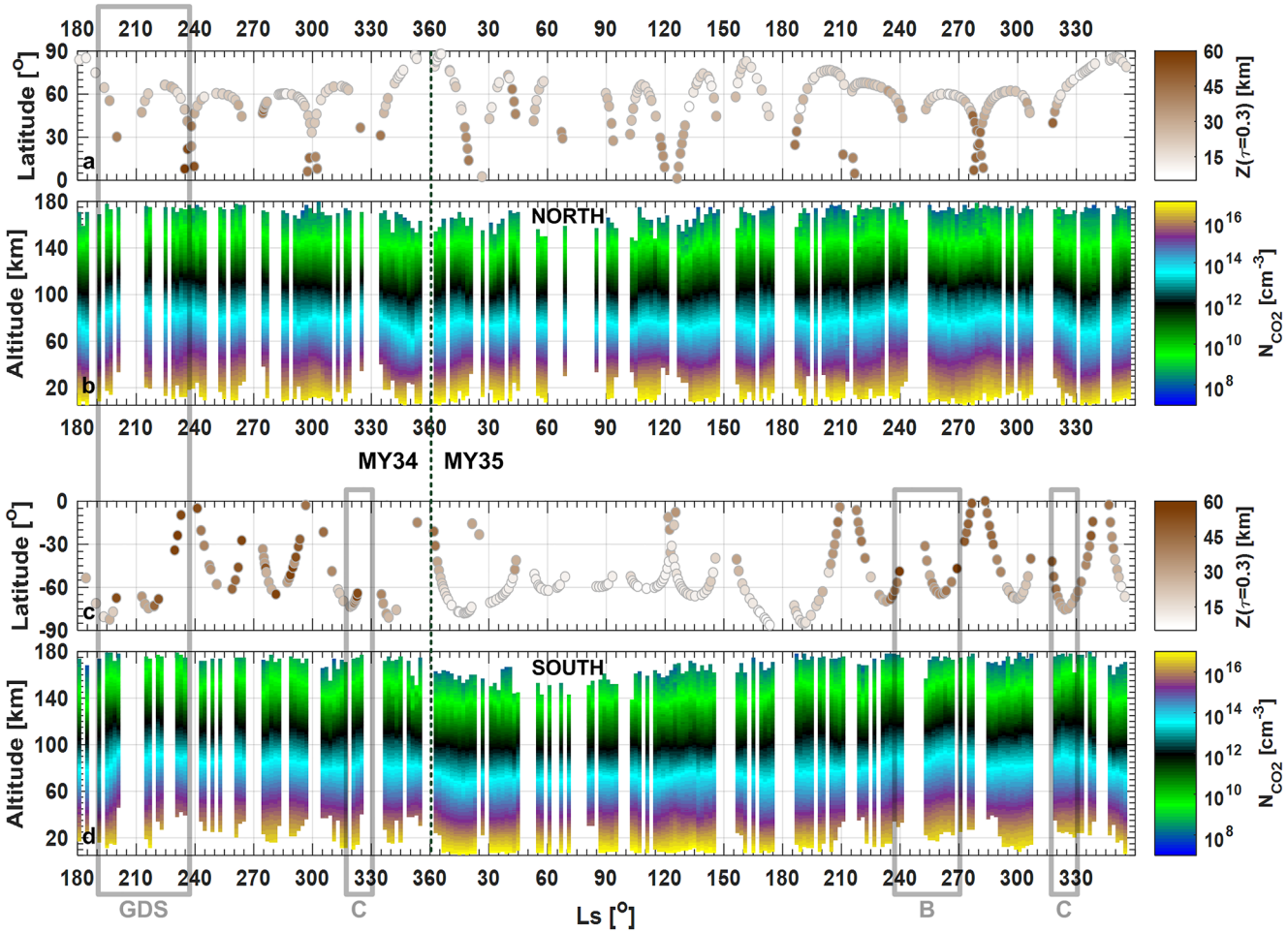

Figure 8. Solar longitude (L_S) cross-sections of Atmospheric Chemistry Suite MIR temperature profiles, grouped in 2° bins, for the (b) Northern and (d) Southern Hemispheres. The density color code indicates different orders of magnitude on the logarithmic scale. Panels (a and c) Latitudinal distribution of the correspondent occultations colored as an altitude level Z where the aerosol slant opacity (τ) equals 0.3. Gray frames outline periods of the global dust storm and the C storm in MY 34 and the B and C storms in MY 35.

other hand, the ACS MIR density varies rather less, just by 1.5 orders of magnitude: from 10^{11} to $3{\cdot}10^{12}$ cm^{-3} (Figure 7b).

The difference with NGIMS may concern to the determination of the tropospheric eddy diffusion coefficient K_0, which remains uncertain in a large range of values below 35 km, from 10^6 to $4{\cdot}10^7$ cm^2/s, while the recommended $K_0 = 10^7$ cm^2/s (Rosenqvist and Chassefière, 1995). Another reason of the discrepancy is an increased solar flux in 2015 during dayside NGIMS measurements rather than our twilight occultations close to the solar minimum during 2018–2020 (S. W. Bougher et al., 2015; Thiemann et al., 2018). This version may explain the large range of the homopause CO_2 density variations (3 orders of magnitude) observed by NGIMS.

4.3. Climatology of CO_2 Density Vertical Distribution

In order to study the seasonal variability of different atmospheric layers we grouped the vertical profiles in bins with intervals of 2° of L_S and 2 km of altitude. In such a way, each bin represents the weighted mean value from one to seven measured points. The points with 1-sigma temperature uncertainties larger than 20 K or relative density deviations exceeding 50% were excluded from consideration. The second rejection criterion corresponds to the detection limit of CO_2 number density (~$5{\cdot}10^7$ cm^{-3}) that defines the seasonal variations of the uppermost detectable points. The distribution of CO_2 number density over 1.5 MYs is shown in Figure 8 for the Northern (Figure 8b) and Southern (Figure 8d) Hemispheres, separately. Those pictures are supplemented by the latitude

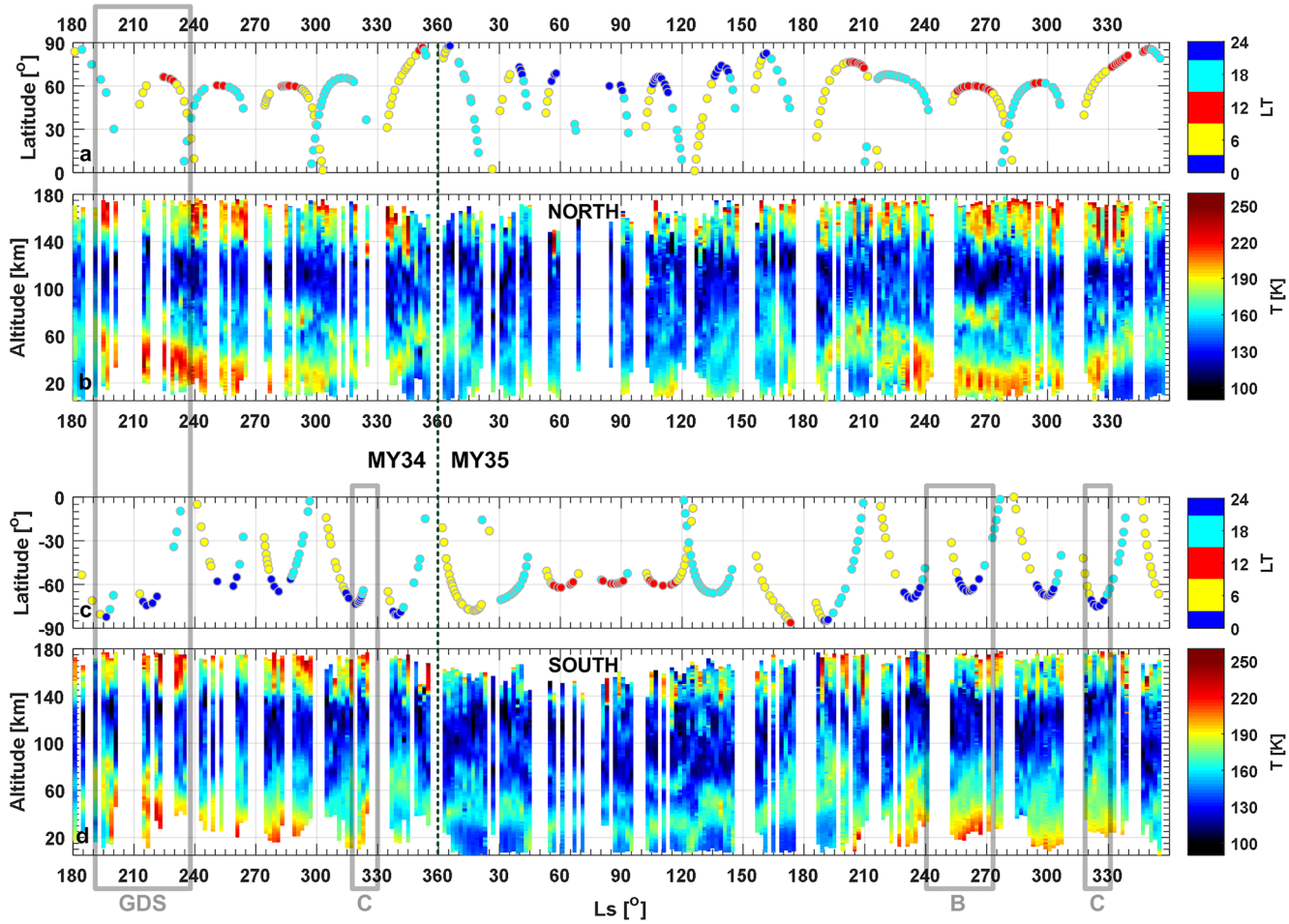

Figure 9. Solar longitude (L_S) cross-sections of Atmospheric Chemistry Suite MIR temperature profiles, grouped in 2° bins, for the (b) Northern and (d) Southern Hemispheres. Panels (a and c) Latitudinal distribution of the correspondent occultations colored by local time: Morning (yellow), day (red), evening (purple), and night (blue). Gray frames outline periods of the global dust storm (GDS) and the C storm in MY 34 and the B and C storms in MY 35.

coverage of individual occultations (Figures 8a and 8c) with corresponding aerosol loading. High latitude coordinates of the ACS MIR occultations just partially caught the dust storms, which are mostly concentrated near equator (Montabone et al., 2020). Nevertheless, we can observe an altitude increase of several density layers during the dust events, especially in the Southern Hemisphere (Figures 8c and 8d).

Generally, seasonal variability for different density layers can be observed in Figure 8. For example, a level of $\sim 10^{12}$ cm^{-3} (the black area), related to the mesopause and homopause layers, varies from 90–100 km at aphelion (L_S = 60°–120°) to 120–130 km at perihelion (L_S = 240°–300°). In parallel, the latitudinal variations of the density altimetry is seen during the equinox seasons (L_S = 330°–30° and L_S = 160°–220°). On the average, we observe a decrease of the altitudes of equivalent CO_2 density layers from the equator to poles, during both spring and autumn seasons. The latitude cross-sections of CO_2 density are shown in Figure S3 in Supporting Information S1. This behavior is expected due to an effect of general polar-to-equatorial atmospheric expansion during equinoxes that coincides with MCD (Millour et al., 2018), as seen in Figures S3c and S3d in Supporting Information S1.

4.4. Climatology of Temperature Vertical Distribution

Seasonal variations of the temperature vertical profiles (Figure 9) were grouped in the same manner as for CO_2 density (Figure 8). In the current case, the distributions are supplemented by the latitudinal coverage color coded by the LT (Figures 9a and 9c) in order to distinguish the thermal structures between the morning and evening

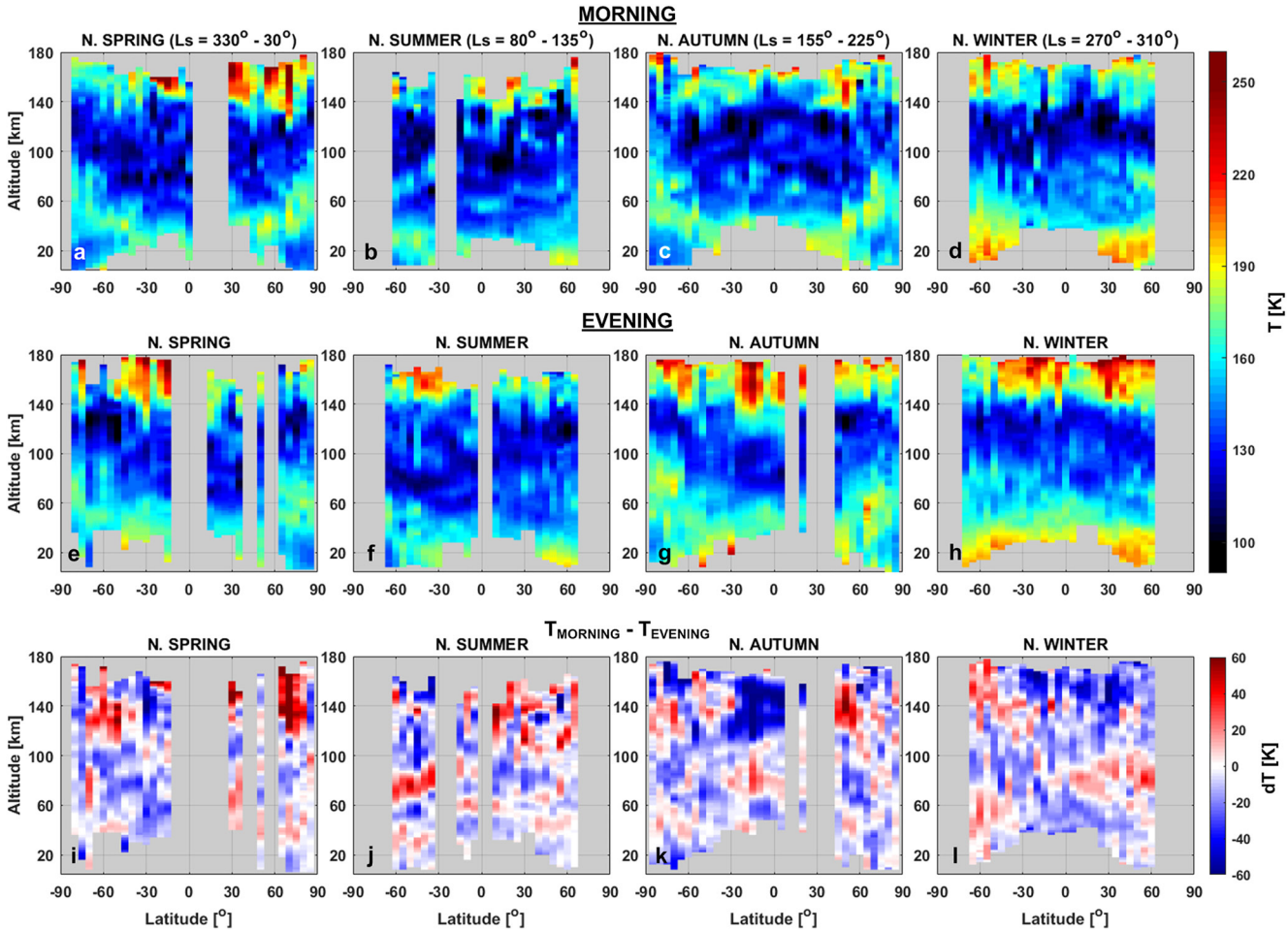

Figure 10. Latitude cross-sections of Atmospheric Chemistry Suite MIR temperature profiles, grouped in 5° bins corresponding seasons: (a, e, and i) Nor. spring (L_S = 330°–30°), (b, f, and j) nor. summer (L_s = 80°–135°), (c, g, and k) nor. autumn (L_S = 155°–225°), and (d, h, and l) nor. winter (L_S = 270°–310°). The data are separated for the (a–d) morning and (e–h) evening terminators with their temperature difference $T_{MORNING} - T_{EVENING}$ (i–l).

twilight. The seasonal temperature variability is presented in Figure 9b for the Northern Hemisphere and in Figure 9d for the Southern one. We observe peak temperatures in the middle atmosphere (40–80 km) during the GDS of MY 34 and a few smaller peaks at the regional B and C storms, regardless of their locations in high southern latitudes and close to the polar night time (Figures 9c and 9d). Apart from the distributions observed during the stormy periods, the middle atmosphere at perihelion (L_S = 240°–300°) is generally warmer than at aphelion (L_S = 60°–120°). Other mesospheric temperature peaks take place locally, depending on latitude. An example is the polar warming effect revealed near the equinox points (L_S = 330°–360° and L_S = 190°–210°). The upper atmosphere features variations of the mesopause level at 70–140 km, indicating the coldest (dark blue) area in Figures 9b and 9d (see also Figure 5). Above the mesopause, we observe the thermospheric temperature rise up to 250–260 K in the warmest case above 150 km.

Analyzing the latitudinal distribution of temperature, we combine the profiles together from MY 34 and MY 35 due to seasons in the Northern Hemisphere (Figure 10): Spring (L_S = 330°–30°), summer (L_S = 80°–135°), autumn (L_S = 155°–225°), and winter (L_S = 270°–310°). The time intervals of stormy events are excluded from the consideration in order to make the equivalent contributions between both Martian years. The L_S periods of summer and autumn are taken as long as possible, in order to consider larger latitude coverage in those season. We also separate the data relative to midday (LT) due to the difference between morning and evening terminators, as shown in Figure 2a.

The mentioned mesospheric polar warming up to 160–190 K occurs at altitudes 50–90 km during spring and autumn symmetrically in both hemispheres and independently on LT (Figures 10a, 10c, 10e and 10g). Below

those warming areas, local temperature minima called "polar vortices" are observed as well. The pronounces warm and cold features at equinoxes were also characterized by MCS measurements (McCleese et al., 2010) and recently by ACS NIR occultations when studying H_2O saturation conditions (Fedorova et al., 2022). The SPICAM stellar occultations demonstrated a polar warming on the night side at altitudes below the mesopause during the period L_S = 120°–150° (Forget et al., 2009). Our observations in this interseasonal interval reach latitudes not higher than 70° in both hemispheres (see Figure 9) with consistent warming, up to 150–170 K below the mesopause.

The difference between morning and evening temperatures (Figures 10i–10l) also reveals some warmer (or colder) layers. Thus, the northern spring thermosphere above ∼120 km is 20–60 K warmed in the morning than in the evening (Figure 10i) and, inversely, colder during the southern spring (Figure 10k). An asymmetry between the hemispheres is revealed during the solstice seasons, as it was also observed by MCS and ACS NIR below 100 km (Fedorova et al., 2022; McCleese et al., 2010). In the thermosphere around 140–180 km, the morning summer at middle-high latitudes of both hemispheres is warmer than the evening one: 220–260 K versus 190–200 K, respectively (Figures 10j and 10l). The Martian global climate model interprets this difference on both Poles in the thermosphere as a result of intense global circulation and in situ tides (González-Galindo et al., 2009, 2015). Comparing between both solstices, the thermospheric northern winter (perihelion, Figures 10d and 10h) is observed to be warmer, up to 200–220 K, than the southern one (aphelion, Figure 10f), up to 180–190 K. Before, the MGS aerobraking around 120 km also revealed the warmer perihelion winter (L_S ∼ 270° and ∼160 K) than the aphelion winter (L_S ∼ 90° and ∼140 K) (S. W. Bougher et al., 2006). The authors explained this behavior by the stronger insolation and dust heating near perihelion. The polar and midlatitude warming up to 250 K at perihelion was also observed by the EUVM/MAVEN solar occultations above 150 km (Thiemann et al., 2018).

The mesosphere also features an explicit morning warming by 20–40 K versus evening at 60–100 km during the winter periods at low-middle latitudes, 60–30°S (Figure 10j) and 0–60°N (Figure 10l), and near equator during the northern autumn, 30°S–10°N (Figure 10k). Those three cases correspond to occultations performed at the maximum LT difference between the morning and evening conditions, close to the semidiurnal period of 12 hr, and during rather short intervals of L_S in MY 35: 115°–130°, 270°–290°, and 205°–225°, respectively (see in Figure 9). Individual temperature profiles observed in those periods are presented in Figure S4 in Supporting Information S1 together with corresponding MCD data. There, most of the measured morning profiles possess temperature bumps at heights 60–90 km that are 20–40 K warmer than those at evening. Analogous patterns were detected by the IUVS/MAVEN stellar occultations at similar altitudes on the night side during aphelion of MY 33 and MY 34 (Nakagawa et al., 2020). Those night temperature profiles revealed the warm layer, up to ∼90 K relative to the MCD predictions, at low-middle northern latitudes that is the case of our perihelion morning observations (Figure 10l and Figure S4c in Supporting Information S1). There are two interpretations of such a phenomenon: Either diurnal thermal tides as modeled by González-Galindo et al. (2015) and also observed by ACS NIR (Fedorova et al., 2022) or stationary planetary waves (Medvedev & Yiğit, 2019).

5. Discussions and Conclusions

For the first time, we report the atmospheric density and temperature retrievals in an extremely broad altitude range from 20 to 180 km on a basis of the CO_2 infrared absorption spectroscopy in the Martian atmosphere. We have used solar occultation measurements by the ACS MIR spectrometer, which is highly sensitive to the strong rotational absorption band of carbon dioxide at the wavelength of 2.7 μm. The retrieval scheme of the transmission spectra include the simultaneous characterization of the CO_2 density and temperature vertical profiles under the assumption of hydrostatic equilibrium. We have processed more than 600 occultation sessions encompassing different seasons over 1.5 MY, the second half of MY 34 and the whole of MY 35. This allowed deriving the seasonal and latitudinal climatology of the density and temperature profiles in both hemispheres and either at morning or at evening terminators.

In the behavior of different atmospheric layers, we can highlight the following features:

- The temperature and CO_2 density in the lower-middle atmosphere (below ∼100 km) increase seasonally: During several dust events, including GDS at L_S = 190°–240° in MY 34 and further B and C storms in MY 35, and in periods of perihelion. This behavior is expected due to the nominal atmospheric expansion at those seasons.

- The mesopause altitude varies in a large range, rising from 70 to 90 km in the winter high latitudes to 130–150 km in the summer high latitudes. Such a high altitude contrast is described by the circulation model of González-Galindo et al. (2009), where interhemispheric meridional winds effectively act around the upper mesosphere and the lower thermosphere, driving the airmass from the summer (southern) hemisphere to the winter (northern) one. A few near-equatorial observations reveal the mesopause subfreezing temperatures, significantly below CO_2 frost point. It may indicate high altitude CO_2-ice clouds at ∼100 km that were previously observed at low latitudes by SPICAM and OMEGA spectrometers (Montmessin et al., 2006, 2007).
- The homopause altitude varies between aphelion and perihelion from 100–110 km to 110–120 km in the Northern Hemisphere, and, more widely, from 90–100 km to 120–130 km in the Southern Hemisphere. Some local extrema are observed depending on dust activity, with maximum at 135 km, and on latitude, with minimum at 85 km in the northern polar equinox. The homopause is generally located above the mesopause at low-middle latitudes, and below the mesopause near polar regions. The correspondent CO_2 density at the homopause changes from 10^{11} to $3{\cdot}10^{12}$ #/cm^3, while the eddy diffusion coefficient occurred to vary from 10^8 cm^2/s at the lowest homopause altitude to $3{\cdot}10^9$ cm^2/s at the uppermost one. Variability of these values coincide with the NGIMS/MAVEN data, which revealed even higher magnitude variations (Slipski et al., 2018).
- The observed symmetrical mesospheric polar warming up to 160–190 K at altitudes 50–90 km during both spring and autumn equinoxes coincides well with the similar thermal structure defined by MSC (McCleese et al., 2010). In the thermosphere, at 140–180 km, such a warming is observed on both northern and southern winter seasons at the middle-high latitudes. The difference between the morning and evening temperatures reveal seasonal warm layers at low-middle latitudes in the mesosphere, 60–100 km. That might be due to the effect of diurnal thermal tides, which is also observed by IUVS/MAVEN on the night side (Nakagawa et al., 2020).

All in all, we have presented a wide diagnostic potential for the troposphere, the mesosphere, and the thermosphere of Mars by the ACS MIR spectroscopy at the CO_2 2.7 μm band. The retrieved data set in the middle and upper atmosphere can serve as a reference for comparison with existing circulation models, for example, one of González-Galindo et al. (2015), of Medvedev et al. (2015), or with the 1D-model of Krasnopolsky et al. (2019), and improve them. In particular, the observed effects of polar warming have been already predicted by those models and could be compared quantitatively. A profound analysis for the mentioned peculiar points, such as mesopause, homopause, or CO_2 frost, could be a subject of further separate papers including an additional statistics from MY 36.

Data Availability Statement

The data sets generated by the ExoMars Trace Gas Orbiter instruments analyzed in this study are available in the ESA Planetary Science Archive (PSA) repository, https://archives.esac.esa.int/psa/%23%21Table%20View/ACS%3Dinstrument, following a 6 months prior access period, following the ESA Rules on Information, Data, and Intellectual Property. The data products generated in this study (retrieved CO_2 density and temperature distributions) are available on Belyaev (2022).

Acknowledgments
ExoMars is a joint space mission of the European Space Agency (ESA) and Roscosmos. The ACS experiment is led by the Space Research Institute (IKI) in Moscow, assisted by LATMOS in France. The analysis of temperature and density profiles at IKI is funded by the Grant 20-42-09035 of the Russian Science Foundation. Oxford participants acknowledge funding from the UK Space Agency (ST/T002069/1) for the data validation.

References

Alday, J., Trokhimovskiy, A., Irwin, P. G. J., Wilson, C. F., Montmessin, F., Lefevre, F., et al. (2021). Isotopic fractionation of water and its photolytic products in the atmosphere of Mars. *Nature Astronomy*, *5*(9), 943–950. https://doi.org/10.1038/s41550-021-01389-x

Alday, J., Wilson, C. F., Irwin, P. G. J., Olsen, K. S., Baggio, L., Montmessin, F., et al. (2019). Oxygen isotopic ratios in Martian water vapor observed by ACS MIR on board the ExoMars Trace Gas Orbiter. *Astronomy and Astrophysics*, *630*, A91. https://doi.org/10.1051/0004-6361/201936234

Alday, J., Wilson, C. F., Irwin, P. G. J., Trokhimovskiy, A., Montmessin, F., Fedorova, A. A., et al. (2021). Isotopic composition of CO_2 in the atmosphere of Mars: Fractionation by diffusive separation observed by the ExoMars trace gas orbiter. *Journal of Geophysical Research: Planets*, *126*(12), e2021JE006992. https://doi.org/10.1029/2021JE006992

Avduyevskiy, V. S., Akim, E. L., Aleshin, V. I., Borodin, N., Kerzhanovich, V., Malkov, Y., et al. (1975). Martian atmosphere in the landing site of the descent module of Mars-6. *NASA transl. into English from Kosm. Issled. (USSR)*, *13*, 21–32.

Belyaev, D. (2022). *Thermal Structure of the Middle and upper Atmosphere of Mars from ACS/TGO CO_2 spectroscopy*. Mendeley Data. V2. https://doi.org/10.17632/g6j5t2z73z.2

Belyaev, D. A., Fedorova, A. A., Trokhimovskiy, A., Alday, J., Montmessin, F., Korablev, O. I., et al. (2021). Revealing a high water abundance in the upper mesosphere of Mars with ACS onboard TGO. *Geophysical Research Letters*, *48*(10), e2021GL093411. https://doi.org/10.1029/2021GL093411

Bougher, S., Jakosky, B., Halekas, J., Grebowsky, J., Luhmann, J., Mahaffy, P., et al. (2015). Early MAVEN Deep Dip campaign reveals thermosphere and ionosphere variability. *Science*, *350*(6261), aad0459. https://doi.org/10.1126/science.aad0459

Bougher, S. W., Bell, J. M., Murphy, J. R., Lopez-Valverde, M. A., & Withers, P. G. (2006). Polar warming in the Mars thermosphere: Seasonal variations owing to changing insolation and dust distributions. *Geophysical Research Letters*, *33*(2), L02203. https://doi.org/10.1029/2005GL024059

Bougher, S. W., Brain, D. A., Fox, J., Gonzalez-Galindo, F., Simon-Wedlund, C., & Withers, P. G. (2017). Chapter 14: Upper atmosphere and ionosphere. In B. Haberle, M. Smith, T. Clancy, F. Forget, & R. Zurek (Eds.), *The atmosphere and climate of Mars*. Cambridge University Press. https://doi.org/10.1017/9781107016187

Bougher, S. W., Pawlowski, D., Bell, J. M., Nelli, S., McDunn, T., Murphy, J. R., et al. (2015). Mars Global Ionosphere-Thermosphere Model (MGITM): Solar cycle, seasonal, and diurnal variations of the Mars upper atmosphere. *Journal of Geophysical Research: Planets*, *120*(2), 311–342. https://doi.org/10.1002/2014JE004715

Bougher, S. W., Roeten, K., Olsen, K., Mahaffy, P. R., Benna, M., Elrod, M., et al. (2017). The structure and variability of Mars dayside thermosphere from MAVEN NGIMS and IUVS measurements: Seasonal and solar activity trends in scale heights and temperatures. *Journal of Geophysical Research: Space Physics*, *122*(1), 1296–1313. https://doi.org/10.1002/2016JA023454

Devi, V. M., Benner, D. C., Sung, K., Crawford, T. J., Gamache, R. R., Renaud, C. L., et al. (2017). Line parameters for CO_2- and self-broadening in the $\nu 3$ band of $HD^{16}O$. *Journal of Quantitative Spectroscopy and Radiative Transfer*, *203*, 158–174. https://doi.org/10.1016/j.jqsrt.2017.02.020

Fedorova, A. A., Montmessin, F., Korablev, O., Luginin, M., Trokhimovskiy, A., Belyaev, D. A., et al. (2020). Stormy water on Mars: The distribution and saturation of atmospheric water during the dusty season. *Science*, *367*(6475), 297–300. https://doi.org/10.1126/science.aay9522

Fedorova, A. A., Montmessin, F., Trokhimovskiy, A., Luginin, M., Korablev, O. I., Alday, J., et al. (2022). A two-Martian year survey of the water vapor saturation state on Mars based on ACS NIR/TGO occultations. *Journal of Geophysical Research, this issue*. https://doi.org/10.1002/essoar.10511229.1

Forbes, J. M., Bruinsma, S., Zhang, X., Forget, F., Marty, J.-C., Millour, E., & Gonsalez-Galindo, F. (2021). The wave origins of longitudinal structures in ExoMars Trace Gas Orbiter (TGO) aerobraking densities. *Journal of Geophysical Research: Space Physics*, *126*(2), e2020JA028769. https://doi.org/10.1029/2020JA028769

Forget, F., Montmessin, F., Bertaux, J.-L., González-Galindo, F., Lebonnois, S., Quémerais, E., et al. (2009). Density and temperatures of the upper Martian atmosphere measured by stellar occultations with Mars Express SPICAM. *Journal of Geophysical Research*, *114*(E1), E01004. https://doi.org/10.1029/2008JE003086

Fu, M. H., Cui, J., Wu, X. S., Wu, Z. P., & Li, J. (2020). The variations of the Martian exobase altitude. *Earth Planetary Physics*, *4*(1), 4–10. https://doi.org/10.26464/epp2020010

Gamache, R. R., Farese, M., & Renaud, C. L. (2016). A spectral line list for water isotopologues in the 1100–4100 cm^{-1} region for application to CO_2-rich planetary atmospheres. *Journal of Molecular Spectroscopy*, *326*, 144–150. https://doi.org/10.1016/j.jms.2015.09.001

González-Galindo, F., Forget, F., Lopez-Valverde, M. A., & Angelats i Coll, M. (2009). A ground-to-exosphere Martian general circulation model: 2. Atmosphere during solstice conditions—Thermospheric polar warming. *Journal of Geophysical Research*, *114*(E8), E08004. https://doi.org/10.1029/2008JE003277

González-Galindo, F., Lopez-Valverde, M. A., Forget, F., Garcia-Comas, M., Millour, E., & Montabone, L. (2015). Variability of the Martian thermosphere during eight Martian years as simulated by a ground-to-exosphere global circulation model. *Journal of Geophysical Research: Planets*, *120*(11), 2020–2035. https://doi.org/10.1002/2015je004925

Gordon, I. E., Rothman, L. S., Hill, C., Kochanov, R. V., Tan, Y., Bernath, P. F., et al. (2017). The HITRAN2016 molecular spectroscopic database. *Journal of Quantum Spectroscopy and Radiative Transfer*, *203*, 3–69. https://doi.org/10.1016/j.jqsrt.2017.06.038

Gröller, H., Montmessin, F., Yelle, R. V., Lefevre, F., Forget, F., Schneider, N. M., et al. (2018). MAVEN/IUVS stellar occultation measurements of Mars atmospheric structure and composition. *Journal of Geophysical Research: Planets*, *123*(6), 1449–1483. https://doi.org/10.1029/2017JE005466

Jacobson, M. Z. (2005). *Fundamentals of atmospheric modeling* (2nd ed.). Cambridge University Press. https://doi.org/10.1017/CBO9781139165389

Jain, S. K., Soto, E., Evans, J. S., Deighan, J., Schneider, N. M., & Bougher, S. W. (2021). Thermal structure of Mars' middle and upper atmospheres: Understanding the impacts of dynamics and solar forcing. *Icarus*, 114703. https://doi.org/10.1016/j.icarus.2021.114703

Jesch, D., Medvedev, A. S., Castellini, F., Yigit, E., & Hartogh, P. (2019). Density fluctuations in the lower thermosphere of Mars retrieved from the ExoMars Trace Gas Orbiter (TGO) aerobraking. *Atmosphere*, *10*, 620. https://doi.org/10.3390/atmos10100620

Keating, G. M., Bougher, S. W., Zurek, R. W., Tolson, R. H., Cancro, G. J., Noll, S. N., et al. (1998). The structure of the upper atmosphere of Mars: In situ accelerometer measurements from Mars Global Surveyor. *Science*, *279*(5357), 1672–1676. https://doi.org/10.1126/science.279.5357.1672

Korablev, O. I., Montmessin, F., Trokhimovskiy, A., Fedorova, A. A., Shakun, A. V., Grigoriev, A. V., et al. (2018). The Atmospheric Chemistry Suite (ACS) of three spectrometers for the ExoMars 2016 trace gas orbiter. *Space Science Reviews*, *214*(1), 7. https://doi.org/10.1007/s11214-017-0437-6

Krasnopolsky, V. A. (2019). *Spectroscopy and photochemistry of planetary atmospheres and ionospheres: Mars, Venus, Titan, and Pluto*. Cambridge University Press. https://doi.org/10.1017/9781316535561

McCleese, D. J., Heavens, N. G., Schofield, J. T., Abdou, W. A., Bandfield, J. L., Calcutt, S. B., et al. (2010). Structure and dynamics of the Martian lower and middle atmosphere as observed by the Mars Climate Sounder: Seasonal variations in zonal mean temperature, dust, and water ice aerosols. *Journal of Geophysical Research*, *115*(E12), E12016. https://doi.org/10.1029/2010JE003677

Medvedev, A. S., González-Galindo, F., Yiğit, E., Feofilov, A. G., Forget, F., & Hartogh, P. (2015). Cooling of the Martian thermosphere by CO_2 radiation and gravity waves: An intercomparison study with two general circulation models. *Journal of Geophysical Research: Planets*, *120*(5), 913–927. https://doi.org/10.1002/2015JE004802

Medvedev, A. S., & Yiğit, E. (2019). Gravity waves in planetary atmospheres: Their effects and parameterization in global circulation models. *Atmosphere*, *10*(9), 531. https://doi.org/10.3390/atmos10090531

Millour, E., Forget, F., Spiga, A., Vals, M., Zakharov, V., Montabone, L., et al. (2018). The Mars climate database (version 5.3). The Mars climate database science workshop "from Mars express to ExoMars". held 27-28 February 2018 at ESAC, Spain, id.68. Retrieved from https://www.cosmos.esa.int/documents/1499429/1583871/Millour_E.pdf/ca419d58-4c0b-29a4-23a9-7c814b5e889e?t=1516102807000

Montabone, L., Spiga, A., Kass, D. M., Kleinböhl, A., Forget, F., & Millour, E. (2020). Martian Year 34 column dust climatology from Mars Climate Sounder observations: Reconstructed maps and model simulations. *Journal of Geophysical Research: Planets*, *125*(8), e06111. https://doi.org/10.1029/2019JE006111

Montmessin, F., Bertaux, J.-L., Quémerais, E., Korablev, O., Rannou, P., Forget, F., et al. (2006). Subvisible CO_2 ice clouds detected in the mesosphere of Mars. *Icarus*, *183*(2), 403–410. https://doi.org/10.1016/j.icarus.2006.03.015

Montmessin, F., Gondet, B., Bibring, J.-P., Langevin, Y., Drossart, P., Forget, F., & Fouchet, T. (2007). Hyperspectral imaging of convective CO_2 ice clouds in the equatorial mesosphere of Mars. *Journal of Geophysical Research*, *112*(E11), E11S90. https://doi.org/10.1029/2007JE002944

Nakagawa, H., Jain, S. K., Schneider, N. M., Montmessin, F., Yelle, R. V., Jiang, F., et al. (2020). A warm layer in the nightside mesosphere of Mars. *Geophysical Research Letters*, *47*(4), e2019GL085646. https://doi.org/10.1029/2019GL085646

Nier, A. O., & McElroy, M. B. (1977). Composition and structure of Mars' upper atmosphere: Results from the neutral mass spectrometers on Viking 1 and 2. *Journal of Geophysical Research*, *82*(28), 4341–4349. https://doi.org/10.1029/JS082i028p04341

Olsen, K. S., Trokhimovskiy, A., Montabone, L., Fedorova, A. A., Luginin, M., Lefèvre, F., et al. (2021). Seasonal reappearance of HCl in the atmosphere of Mars during the Mars year 35 dusty season. *Astronomy & Astrophysics*, *647*, A161. https://doi.org/10.1051/0004-6361/202140329

Piccialli, A., Montmessin, F., Belyaev, D., Mahieux, A., Fedorova, A., Marcq, E., et al. (2015). Thermal structure of Venus nightside upper atmosphere measured by stellar occultations with SPICAV/Venus Express. *Planetary and Space Science*, *113–114*, 321–335. https://doi.org/10.1016/j.pss.2014.12.009

Quemerais, E., Bertaux, J. L., Korablev, O., Dimarellis, E., Cot, C., Sandel, B. R., & Fussen, D. (2006). Stellar occultations observed by SPICAM on Mars Express. *Journal of Geophysical Research*, *111*(E9), E09S04. https://doi.org/10.1029/2005JE002604

Rosenqvist, J., & Chassefière, E. (1995). A reexamination of the relationship between eddy mixing and O_2 in the Martian middle atmosphere. *Journal of Geophysical Research*, *100*(E3), 5541. https://doi.org/10.1029/95je00324

Seiff, A., & Kirk, D. B. (1976). Structure of Mars' atmosphere up to 100 kilometers from the entry measurements of Viking 2. *Science*, *194*(4271), 1300–1303. https://doi.org/10.1126/science.194.4271.1300

Slipski, M., Jakosky, B. M., Benna, M., Elrod, M., Mahaffy, P., Kass, D., et al. (2018). Variability of Martian turbopause altitudes. *Journal of Geophysical Research: Planets*, *123*(11), 2939–2957. https://doi.org/10.1029/2018JE005704

Stone, S., Yelle, R. V., Benna, M., Elrod, M. K., & Mahaffy, P. R. (2018). Thermal structure of the Martian upper atmosphere from MAVEN NGIMS. *Journal of Geophysical Research: Planets*, *123*(11), 2842–2867. https://doi.org/10.1029/2018JE005559

Thiemann, E. M. B., Eparvier, F. G., Bougher, S. W., Dominique, M., Andersson, L., Girazian, Z., et al. (2018). Mars thermospheric variability revealed by MAVEN EUVM solar occultations: Structure at aphelion and perihelion and response to EUV forcing. *Journal of Geophysical Research: Planets*, *123*(9), 2248–2269. https://doi.org/10.1029/2018JE005550

Vandaele, A.-C., Lopez-Moreno, J. J., Patel, M. R., Bellucci, G., Daerden, F., Ristic, B., et al. (2018). NOMAD, an integrated suite of three spectrometers for the ExoMars trace gas mission: Technical description, science objectives and expected performance. *Space Science Reviews*, *214*(5), 80. https://doi.org/10.1007/s11214-018-0517-2

Washburn, E. (1948). *International critical tables of numerical data, Physics, Chemistry, and Technology* (Vol. 3). McGraw-Hill.

Withers, P. (2006). Mars Global surveyor and Mars Odyssey accelerometer observations of the Martian upper atmosphere during aerobraking. *Geophysical Research Letters*, *33*(2), L02201. https://doi.org/10.1029/2005GL024447

Withers, P., Towner, M. C., Hathi, B., & Zarnecki, J. C. (2003). Analysis of entry accelerometer data: A case study of Mars pathfinder. *Planetary and Space Science*, *51*(9–10), 541–561. https://doi.org/10.1016/S0032-0633(03)00077-1

Zurek, R. W., Tolson, R. A., Bougher, S. W., Lugo, R. A., Baird, D. T., Bell, J. M., & Jakosky, B. M. (2017). Mars thermosphere as seen in MAVEN accelerometer data. *Journal of Geophysical Research: Space Physics*, *122*(3), 3798–3814. https://doi.org/10.1002/2016ja023641